Vibrational entropies of oxygen vacancy formation in metal oxides

Bianca Baldassarri,[1] Jiangang He,[2,*] and Christopher Wolverton[1,2,†]
[1]*Graduate Program in Applied Physics, Northwestern University, Evanston, Illinois 60208, USA*
[2]*Department of Materials Science and Engineering, Northwestern University, Evanston, Illinois 60208, USA*

(Received 28 October 2023; accepted 30 April 2024; published 30 May 2024)

Oxygen vacancies play a key role in many energy-related applications, and the investigation of the thermodynamic forces driving their formation across different materials can be tackled through the use of *ab initio* methods. In this context, however, computational studies targeting finite-temperature properties such as entropy remain scarce. Wider-ranging studies are of interest to deepen the understanding of the role of the entropy of oxygen vacancy formation and its different components in processes like the ones involved in solar thermochemical hydrogen (STCH) production, and to investigate the existence of common trends and differences between materials. In this work, we use density functional theory and harmonic phonon calculations to compute the vibrational entropy of oxygen vacancy formation (ΔS_{vib}) for 10 different metal oxide compounds. The computation is carried out by taking the difference between the vibrational entropy of a vacancy-containing and a pristine structure, while the entropic contribution from the final gaseous state of the oxygen lost from the material is accounted for separately with a gas entropy term. We first examine the temperature dependence of ΔS_{vib} and highlight the presence of an initial peak around room temperature, followed by a steady decrease resulting from the presence of an additional O atom (the one becoming vacant) in the defect-free structure. We then inspect the atomic contributions to ΔS_{vib}, and highlight similarities and differences between compounds. Finally, we consider other significant sources of entropy, and find ΔS_{vib} to provide a smaller, yet non-negligible, contribution to the total entropy of vacancy formation. We also compare the temperature dependence of ΔS_{vib} to that of the gas entropy, and show that the two largely counterbalance each other at high temperatures.

DOI: 10.1103/PhysRevMaterials.8.055407

I. INTRODUCTION

The formation of oxygen vacancies can have favorable effects for various technologies. Oxygen off-stoichiometry can be advantageous for applications such as photocatalysis [1] and piezocatalysis [2]. In solar-thermochemical hydrogen (STCH) production, the presence of oxygen loss plays a fundamental role, with typical two-step cycles relying on oxygen release at higher temperature to then harvest H_2 upon flowing water vapor in the oxygen-deficient material at lower temperatures [3–7]. Analogous processes relying on oxygen loss for a two-step reduction-oxidation reaction also find applications in air separation [8] and splitting of CO_2 into CO and O_2 [5–7,9,10]. Depending on the technology of interest, target value ranges for the enthalpy and entropy changes involved in the reduction reaction can be identified for the relevant operating conditions [11], and utilized to guide material selection. The energies of oxygen vacancy formation can also be employed to vet candidate materials for applications such as solid oxide fuel cells (SOFCs) [12–14], where oxygen vacancy concentration and mobility determine the diffusion of oxygen ions in the cathode.

Ab initio methods can often represent useful tools for studying materials on a large scale, exploring potential trends and accelerating materials discovery and selection. Several density functional theory (DFT) studies have been dedicated to the computation of oxygen vacancy formation energies (ΔE_{vf}), covering a range of different structure types and a vast array of compositions [15–19]. The availability of sizable data sets of ΔE_{vf} calculations has then offered the possibility of uncovering trends across materials and developing predictive models [15–17,19–21], presenting an even larger potential for materials investigation.

Finite-temperature properties such as the nonconfigurational entropy of oxygen defect formation, however, remain less studied on a computational level. Naghavi *et al.* [22] examined the entropic contribution originating from the coupling between orbital and spin angular momenta in lanthanide ions, finding the reduction of Ce^{4+} ions to result in an exceptionally large value compared to all the other lanthanide atoms, and uncovering a particularly significant contribution to the large entropy of reduction of Ceria, the benchmark material in STCH [23,24]. The solid-state entropy of reduction of Ceria was also at the center of a study by Gopal and van de Walle [25], who computed configurational and vibrational entropic contributions through cluster expansion Hamiltonian-based Monte Carlo simulations. While still investigating defect formation in Ceria, Grieshammer *et al.* [26] targeted the vibrational component alone, examining multiple types of defects including O vacancies. Similar small-scale studies examining the vibrational entropy of O vacancy formation in a specific material of interest have been conducted for a limited number of metal oxide compounds (see, e.g.,

*Present address: School of Mathematics and Physics, University of Science and Technology Beijing, Beijing, China.
†Corresponding author: c-wolverton@northwestern.edu

Refs. [27,28]). Wider-ranging studies than the ones present in the literature are of interest to deepen the understating of the role of the solid-state vibrational entropy of O vacancy formation in processes like the ones involved in STCH, and to investigate common features and differences between materials.

In this study, we examine the change in solid-state vibrational entropy involved in the formation of oxygen vacancies (ΔS_{vib}) in 10 different metal oxide compounds, crystallizing in different structure types: perovskite, double perovskite, hexagonal "$LuMnO_3$"-type, and pyrochlore. We consider the formation of neutral oxygen vacancies, where the final state of oxygen is accounted for with a gaseous entropy term, discussed in the last section of the text. We both highlight common features in ΔS_{vib} between the compounds examined, such as the trend with temperature, and we identify significant differences, such as the contributions from the cations neighboring the vacancy. Examining the mechanisms leading to positive or negative contributions to ΔS_{vib}, we find the lengthening of the bonds between the reducing cations and the neighboring oxygen atoms to lead to an increase in vibrational entropy. We also connect the loss of the O atom with a steady decrease in ΔS_{vib} at higher temperatures. Finally, we compare the change in solid-state vibrational entropy to other significant contributions to the total entropy of vacancy formation, namely the gas entropy of O_2 and the configurational entropy, finding ΔS_{vib} to play a smaller but non-negligible role.

By computing and analyzing the vibrational entropy of defect formation of multiple compounds, the present work allows to draw comparisons of this quantity across compounds, and with other entropic contributions. The text is divided as follows: we first examine the trends in the vibrational entropy of O vacancy formation with temperature in Sec. III A, we then investigate contributions from different atoms in the compounds in Sec. III B, we explore the influence of Hubbard U in Sec. III C, and we consider other sources of entropy in the vacancy formation reaction in Sec. III D.

II. METHODS

All DFT calculations in this work have been conducted using the Vienna ab-initio simulation package (VASP) [29,30], with projector augmented wave (PAW) potentials [31] and the Perdew-Burke-Ernzerhof (PBE) [32] generalized gradient approximation (GGA) for the exchange-correlation functional. A plane-wave cutoff energy of 520 eV was employed, with a gamma centered k-point grid with a density of at least 8600 points per reciprocal atom, and spin polarization was applied with a ferromagnetic configuration, initializing magnetic moments to $5\mu_B$. Self-consistency was achieved when energies of subsequent iterations differed by less than 10^{-6} eV/cell, and ionic relaxation was performed until forces were found to be below 0.001 eV/Å. The over-delocalization of electrons in compounds containing 3d transition metals due to the residual self-interaction present in exchange-correlation functionals [33–37] was treated through the addition of a Hubbard-like potential to the energy functional [38]. Results in Secs. III A and III B are presented for a constant value of $U = 4$ eV for all compounds, but the effect of utilizing different U values is explored in Sec. III C.

Phonon dispersions were calculated by means of the finite-difference method as implemented in PHONOPY [39], where the vibrational entropy is computed as follows:

$$S_{\text{vib}}(T) = \frac{1}{2T}\sum_{\mathbf{q}\nu}\hbar\omega(\mathbf{q}\nu)\coth\left(\frac{\hbar\omega(\mathbf{q}\nu)}{2k_BT}\right) - k_B\sum_{\mathbf{q}\nu}\ln\left[2\sinh\left(\frac{\hbar\omega(\mathbf{q}\nu)}{2k_BT}\right)\right]. \quad (1)$$

The solid-state vibrational entropy of vacancy formation ΔS_{vib} (per O vacancy) was calculated by computing the difference in vibrational entropy between the pristine and vacancy-containing cell, which for an $A_xB_yO_z$ compound can be expressed as

$$\Delta S_{\text{vib}} = S_{\text{vib}}(A_xB_yO_{z-\delta}) - S_{\text{vib}}(A_xB_yO_z), \quad (2)$$

where $S_{\text{vib}}(A_xB_yO_{z-\delta})$ is the vibrational entropy of the defect-containing cell (containing one O vacancy), and $S_{\text{vib}}(A_xB_yO_z)$ is the vibrational entropy of the defect-free cell, both of which are calculated from structures where both volumes and atomic positions are allowed to relax (specifically, the defect-containing structure is obtained by performing a standard relaxation after introducing a vacancy in the relaxed pristine cell). The two cells (pristine and defect-containing) have a different number of atoms, i.e., the pristine cell contains one more oxygen atom (the one becoming vacant) compared to the defect-containing one. The entropy of the final state of the O atom becoming vacant is accounted for through the gas entropy term discussed in more detail in Sec. III D. Note that, while the vibrational entropy of vacancy formation is a function of temperature, we refer to it as ΔS_{vib} instead of $\Delta S_{\text{vib}}(T)$ for short in many instances in the text. The units of ΔS_{vib} utilized in the text are Boltzmann constants per oxygen vacancy.

ΔS_{vib} was computed for 10 different compounds: the orthorhombic perovskites $LaMnO_3$, $CaMnO_3$, $YFeO_3$, and $LaFeO_3$, the B-site ordered double perovskites Sr_2MnTiO_6 and Ca_2MnTiO_6, the "$LuMnO_3$"-type compounds $YMnO_3$, $HoMnO_3$, and $LuMnO_3$, and the pyrochlore $Lu_2Mn_2O_7$ (see Fig. S1 for visual representations of structures). This study aims to investigate the vibrational entropy of oxygen vacancy (V_O) formation associated with more dilute vacancy concentrations, within a reasonable computational cost. For each compound, defective structures were obtained by introducing an O vacancy in supercells of, respectively, 80 atoms for perovskite oxides, 90 atoms for "$LuMnO_3$"-type compounds, and 88 atoms for pyrochlore oxides. The above cell sizes correspond to, respectively, ∼2.1% of O atoms being vacant in perovskites (corresponding to a nonstoichiometry $\delta \sim 0.063$ in $ABO_{3-\delta}$), ∼1.9% of O atoms being vacant in "$LuMnO_3$"-type compounds ($\delta \sim 0.056$ in $ABO_{3-\delta}$), and ∼1.8% of O atoms being vacant in pyrochlore compounds ($\delta \sim 0.125$ in $A_2B_2O_{7-\delta}$). 1×2×1 supercells of the 80-atom cells (where the b axis is shorter than the a and c axes before doubling) were constructed for phonon calculations of perovskite oxides, such that phonon calculations were conducted with cell dimensions $\gtrsim$10 Å along all directions for all compounds. The supercells used have the largest dimensions that could be considered at a reasonable computational cost while maintaining

similar sizes along the three spatial directions. A compound ($HoMnO_3$) was selected to investigate the effects of doubling the size of the phonon supercell in both the pristine and the defective cell, displaying a change of less than $0.1k_B$ (per O vacancy) in the vibrational entropy of vacancy formation (see Fig. S2).

In Sec. III A, in order to investigate the effect of temperature on the contribution from different frequencies to the total vibrational entropy of V_O formation, we compute the running integral of the solid-state vibrational entropy of O vacancy formation, $\Delta S_{\text{vib}}(\omega, T)$. This quantity is computed by only integrating the entropy up to a frequency ω [with $\Delta g(\omega)$ indicating the density-of-states difference between the defective and pristine structures]:

$$\Delta S_{\text{vib}}(\omega, T) = \int_0^{\omega} \left\{ \frac{\hbar\omega}{2T} \coth\left(\frac{\hbar\omega}{2k_BT}\right) - k_B \ln\left[2\sinh\left(\frac{\hbar\omega}{2k_BT}\right)\right] \right\} \Delta g(\omega) d\omega. \quad (3)$$

Including all frequencies in the running integral yields the total entropy ΔS_{vib}.

In Sec. III D, other contributions to the total entropy of V_O formation are examined. As mentioned, ΔS_{vib} only accounts for the change in the solid-state vibrational entropy (at the harmonic level) of the metal oxide upon introducing an O vacancy, and it is calculated as the difference in vibrational entropy between two cells with a different number of atoms (specifically, one less O atom in the defect-containing cell). The vibrational entropy of O in its final gas state is accounted for (alongside other relevant contributions arising from, e.g., translational and rotational degrees of freedom) in the gas entropy term, which can be extracted from tabulated standard values [40] (see the relevant discussion in Sec. III D). We note that the NIST-JANAF tables [40] are constructed including, in addition to the translational, rotational, vibrational, and electronic components, an anharmonic correction. This anharmonic correction, which in any case has a very limited impact on the total entropy of molecular oxygen, is excluded in this text for coherence with the harmonic treatment utilized in our calculations. The total entropy of O vacancy formation can then be calculated as

$$\Delta S_{\text{tot}} = \Delta S_{\text{vib}} + 1/2S(O_2) + \Delta S_{\text{other}}, \quad (4)$$

where $1/2S(O_2)$ represents the gas entropy contribution, and ΔS_{other} accounts for contributions to the total entropy of V_O formation other than the change in solid-state vibrational entropy and the gas entropy. For the compounds examined in this text, we consider the main contribution to ΔS_{other} to be from the configurational entropy, as discussed further in Sec. III D, but other sources of entropy, such as electronic [22] and magnetic can also contribute to the total entropy of V_O formation. The units of the entropy of oxygen gas utilized in the text are Boltzmann constants per atom.

In multiple parts of the discussion, we examine the high-temperature classical behavior of various entropic contributions. The relevant expressions are discussed in the next paragraphs.

The integrand (excluding the density of states) of the vibrational entropy in the high-T limit can be expressed as (leveraging series expansion) [41]

$$\begin{aligned} &\frac{\hbar\omega}{2T}\coth\left(\frac{\hbar\omega}{2k_BT}\right) - k_B\ln\left[2\sinh\left(\frac{\hbar\omega}{2k_BT}\right)\right] \\ &= k_B\left(\frac{\hbar\omega}{k_BT}\frac{1}{e^{\frac{\hbar\omega}{k_BT}}-1} - \ln\left(1-e^{-\frac{\hbar\omega}{k_BT}}\right)\right) \\ &\simeq \ln\left(\frac{k_BT}{\hbar\omega}\right) + 1. \end{aligned} \quad (5)$$

Consequently, the vibrational entropy of vacancy formation can be simplified to

$$\begin{aligned} \Delta S_{\text{vib}} &\simeq k_B \int_0^{\infty} \left[\ln\left(\frac{k_BT}{\hbar\omega}\right) + 1\right] \Delta g(\omega) d\omega \\ &\simeq -k_B \int_0^{\infty} \ln(\hbar\omega)\Delta g(\omega) d\omega + 3k_B\ln(T) \\ &\quad + 3k_B[\ln(k_B) + 1]. \end{aligned} \quad (6)$$

Therefore, at higher temperatures, the temperature dependence of ΔS_{vib} is captured by the term $\Delta S_{\text{vib}}^{T\text{-dep}} = 3k_B\ln(T)$, and the differences between compounds are captured by the term $\Delta S_{\text{vib}}^{T\text{-ind}} = 3k_B[\ln(k_B)+1] - k_B\int_0^{\infty}\ln(\hbar\omega)\Delta g(\omega)d\omega$.

The classical expression for the translational contribution to the entropy of one mole of O_2 gas is given by the Sackur-Tetrode equation [42]:

$$S_{\text{tr}}(O_2) = k_BN_A\left[\ln\left(\frac{V}{N_A}\left(\frac{2\pi mk_BT}{h^2}\right)^{3/2}\right) + \frac{5}{2}\right], \quad (7)$$

where, at standard state pressure, $V = N_Ak_BT/p_0$. Treating the O_2 molecule as a rigid rotor, the rotational contribution (per mole) to the gas entropy can be expressed as [42]

$$S_{\text{rot}}(O_2) = k_BN_A\left[\ln\left(\frac{T}{2\Theta_R}\right) + 1\right], \quad (8)$$

where $\Theta_R = \frac{l^2}{8\pi^2Ik_B}$, with the moment of inertia $I = \mu l^2$ (μ indicating the reduced mass and l the bond length of the O_2 molecule). A harmonic treatment of the vibration of O_2 then leads to the term [42]

$$S_{\text{vib}}(O_2) = k_BN_A\left(\frac{\Theta_V}{T}\frac{1}{e^{\Theta_V/T}-1} - \ln(1-e^{-\Theta_V/T})\right), \quad (9)$$

where $\Theta_V = \hbar\omega_V/k_B$ (ω_V indicating the harmonic vibrational frequency of the O_2 molecule). Expressing the (per mole) oxygen gas entropy as a sum of the above contributions and a term accounting for the multiplicity of the triplet ground state, and simplifying the expression for the vibrational contribution analogously with the high-temperature treatment of ΔS_{vib} outlined in the previous paragraph, we obtain

$$\frac{1}{2}S(O_2) = k_BN_A\left[\frac{9}{4}\ln(T) + \frac{1}{2}\ln\left(\frac{3(2\pi m)^{3/2}k_B^{5/2}}{2\Theta_R\Theta_Vp_0h^3}\right) + \frac{9}{4}\right]. \quad (10)$$

Therefore, at higher temperatures the temperature dependence of $\frac{1}{2}S(O_2)$ is captured by the $\frac{9}{4}k_B\ln(T)$ term.

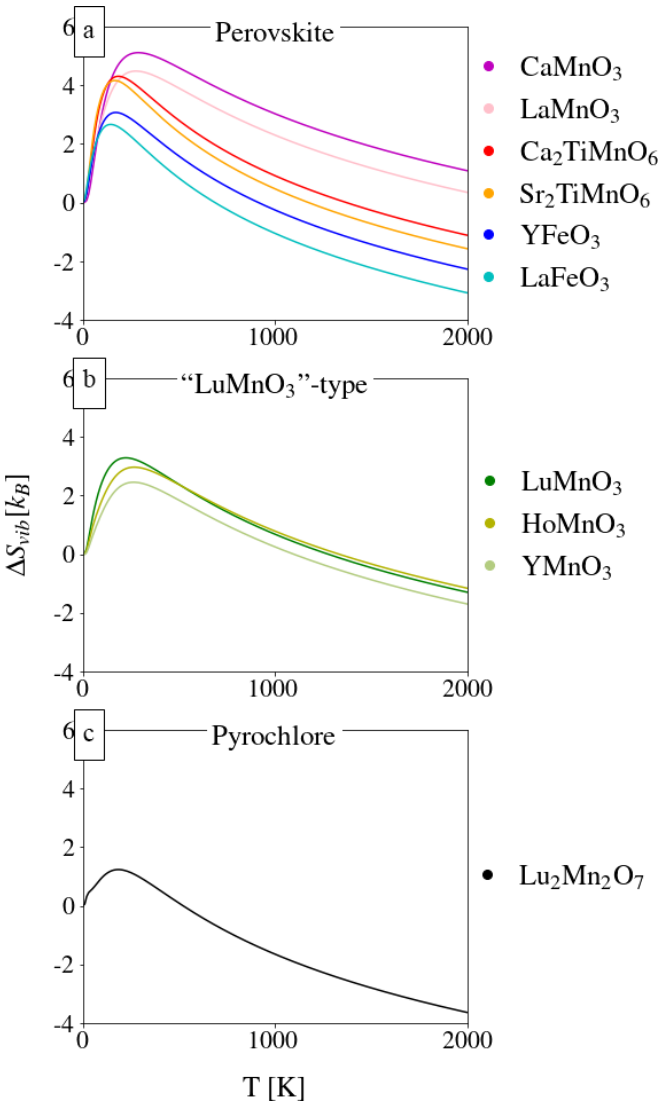

FIG. 1. Solid-state vibrational entropy of O vacancy formation (ΔS_{vib}) as a function of temperature for compounds with (a) a perovskite structure (for which the cell size used in the defective calculation corresponds to ∼2.1% of O atoms being vacant), (b) a "$LuMnO_3$"-type structure (for which the cell size used in the defective calculation corresponds to ∼1.9% of O atoms being vacant), and (c) a pyrochlore structure (for which the cell size used in the defective calculation corresponds to ∼1.8% of O atoms being vacant).

III. RESULTS

In Fig. 1 we compare the solid-state vibrational entropy of V_O formation of all the compounds we selected as a function of temperature, subdividing by structure type: (a) perovskite (displaying the orthorhombic perovskites $LaMnO_3$, $CaMnO_3$, $YFeO_3$, and $LaFeO_3$ and the B-site ordered double perovskites Sr_2MnTiO_6 and Ca_2MnTiO_6), (b) "$LuMnO_3$"-type (displaying $YMnO_3$, $HoMnO_3$, and $LuMnO_3$), and (c) pyrochlore (displaying $Lu_2Mn_2O_7$). We also report the vibrational entropy of each of the above pristine compounds in the Supplemental Material [43] (see Fig. S3). It can be observed that, in all cases, an initial increase in ΔS_{vib} is followed by a peak around room temperature, and then a steady decrease. Despite the general similarities in the overall temperature behavior, differences can be observed between materials, mainly in terms of the height and location of the peak, and of the initial rate of descent. We analyze these behaviors over the next sections. First, in Sec. III A, we rationalize the general shape of the temperature dependence of ΔS_{vib}, identifying the main contributions to each feature of the curve. In Sec. III B we then analyze the different atomic contributions to the vibrational entropy, highlighting similarities and differences between compounds. Finally, in Sec. III D, we examine the configurational and gas phase contributions to the entropy of vacancy formation.

A. Temperature dependence of ΔS_{vib}

As is visible in Fig. 1, two basic components of the trend of ΔS_{vib} with T can be identified: an initial increase and a subsequent decrease. To investigate the origin of these features, we first visualize the differences in the phonon density of states of the pristine and of the vacancy-containing structure and the contributions to the entropy of different vibrational frequency regions at various temperatures. To connect the ΔS_{vib} versus T curve to the contribution from different atoms in the structure, we then also examine their individual contributions to the phonon density of states. As the general features of the ΔS_{vib} versus T curve are common to all compounds we studied, we select one specific compound, $HoMnO_3$, to illustrate density-of-states–related properties.

We start the investigation of the origin of the temperature dependence ΔS_{vib} on T by examining general features of the phonon density of states (DOS) of $HoMnO_3$. In Fig. 2(a) we first compare the DOS of the pristine and defect-containing structure. Several differences can be noticed in the phonon DOS of the defective structure when compared to the pristine one, most notably an additional lower-frequency (∼2 THz) peak and a redshift in the frequencies of states at higher frequencies (∼17 THz). Having compared the two DOS curves (defect-containing and pristine) separately, we then compute their difference, and we integrate it over vibrational frequency, as shown through the black dotted line in Fig. 2(b). The integrated Δ DOS has positive values for all lower frequencies, with then a peak at around 17 THz followed by a decrease to negative values for higher frequencies. To examine how the contribution of different frequencies to the vibrational entropy changes with temperature, we also display in Fig. 2(b) the running integral of the vibrational entropy of vacancy formation, $\Delta S_{\text{vib}}(\omega, T)$ [defined in Eq. (3)], for five different temperature values (identified through different colors). At lower temperatures, the dominant contribution to the vibrational entropy comes from smaller frequencies, where the integrated Δ DOS is positive, which is consistent with the initial growth of ΔS_{vib} with temperature observed in Fig. 1. As temperature increases, however, larger frequencies start to have a larger weight, and, due to the no longer negligible contribution from the frequencies at which the integrated Δ DOS is negative, ΔS_{vib} starts decreasing.

Having identified the main features in the phonon density of states which determine the dependence of ΔS_{vib} on T, we now investigate the source of these features. To do so, we separate the contributions to the phonon band structure

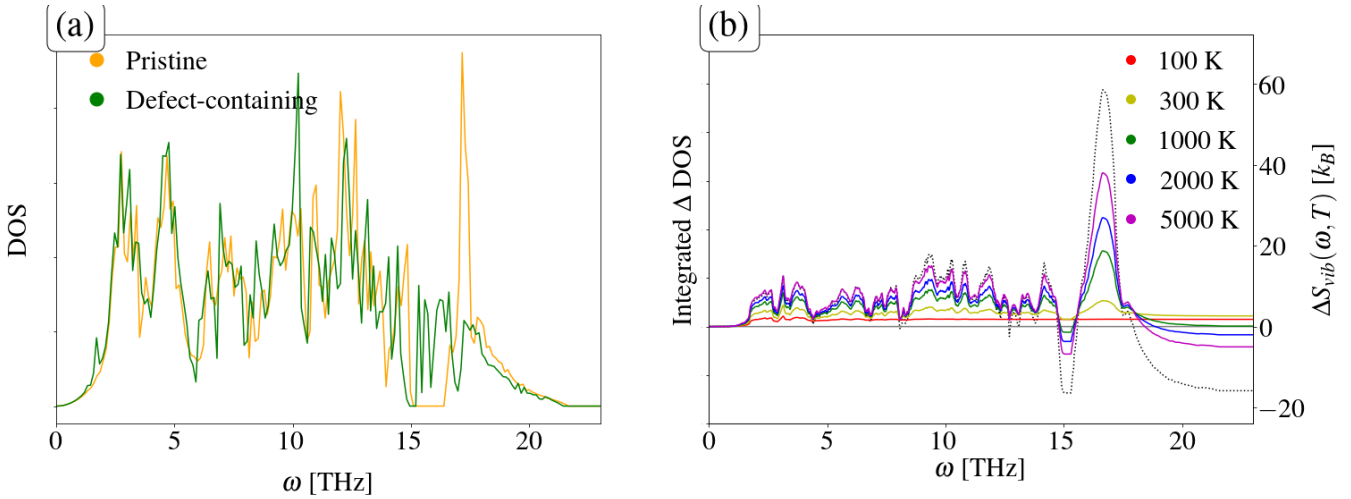

FIG. 2. (a) Phonon density of states of the pristine (orange) and defect-containing (green) structures of $HoMnO_3$. (b) Left-hand y axis: Difference in the density of states between vacancy-containing and pristine structures, integrated over vibrational frequencies (black dotted line). Right-hand y axis: running integral of the vibrational entropy of vacancy formation of $HoMnO_3$, $\Delta S_{\text{vib}}(\omega, T)$ [see Eq. (3)], obtained by taking the vibrational entropy difference between the pristine and vacancy-containing structure of $HoMnO_3$ including only contributions up to the vibrational frequency value indicated in the x axis (solid lines of different colors indicating different temperatures).

from the different atoms in the structure. In Fig. 3, we display the atom projected phonon density of states (PDOS) of (a) the pristine structure and (b) the vacancy-containing structure of $HoMnO_3$. In the low-frequency region, the contributions from the heaviest (in this case Ho) atoms dominate, while O, being the lightest species, is mainly associated with the higher-frequency region. In general, it can be seen that the change in the phonon spectrum upon defect formation is not localized, but rather differences along various frequency ranges can be seen between pristine and defect-containing structures. As will be further detailed in the next section, such differences can be principally associated with the metal cations neighboring the vacancy and the oxygen atoms bonded to them. The low-frequency peak observed in the defect DOS in Fig. 2(a) is associated with a redshift of the vibrational frequency of the Ho atom neighboring the vacancy, which is consistent with bond-breaking. A similar redshift is also associated with the vibrational frequencies of the Mn atoms neighboring the vacancy. We consider both such redshifts to be connected with the initial positive value of the integrated Δ DOS and of ΔS_{vib}. As for the oxygen atoms, a redshift upon vacancy formation can also be observed in the region ∼15–17 THz, which is responsible for the peak in the integrated DOS. However, the higher density of states in the pristine structure at larger frequencies (∼18 THz), which we also associate with the presence of one additional oxygen atom (the one becoming vacant) in the pristine structure, eventually dominates leading to a decrease in ΔS_{vib}.

The high-temperature behavior of ΔS_{vib} for all compounds can be further understood and simplified, considering two

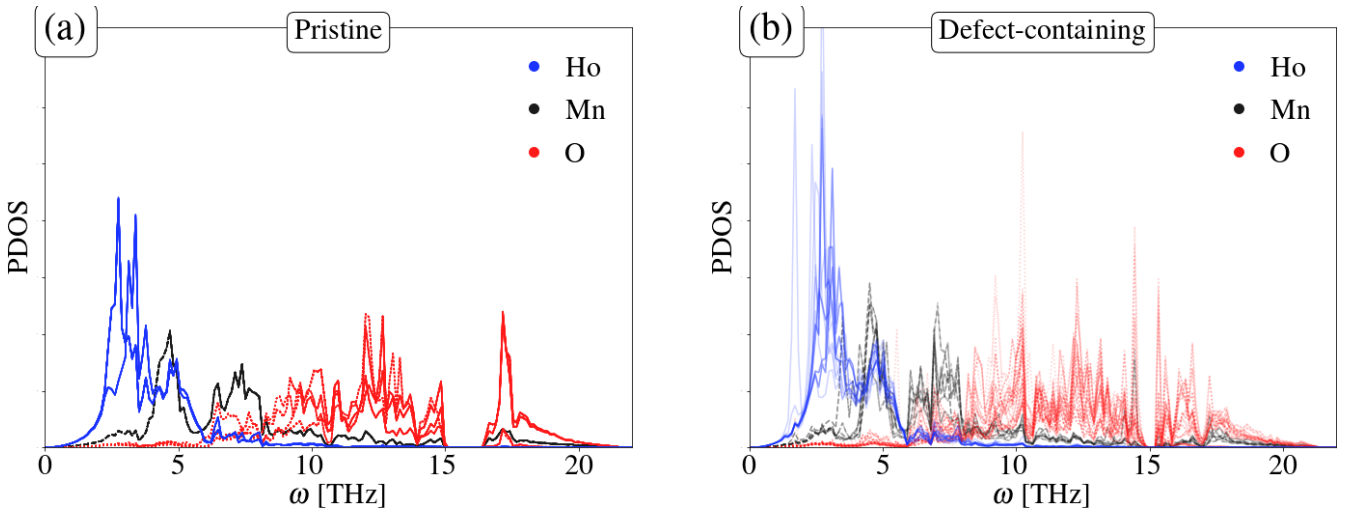

FIG. 3. Atom projected phonon density of states of (a) the pristine structure and (b) the vacancy-containing structure of $HoMnO_3$. Red dotted lines represent contributions from O atoms, gray dashed lines represent contributions from Mn atoms, and blue solid lines represent contributions from Ho atoms.

TABLE I. Temperature-independent component of the high-temperature solid-state vibrational entropy of O vacancy formation [see Eq. (6)] for the 10 compounds included in the study.

Composition	$\Delta S_{\text{vib}}^{T\text{-ind}}[k_B]$
$CaMnO_3$	23.9
$LaMnO_3$	23.1
$LuMnO_3$	21.5
$HoMnO_3$	21.6
$YMnO_3$	21.1
$Ca_2TiMnO6$	21.7
$Sr_2TiMnO6$	21.2
$YFeO_3$	20.6
$LaFeO_3$	19.7
$Lu_2Mn_2O_7$	19.1

main contributions: a T-dependent term that is equal for all compounds, corresponding to $3k_B\ln(T)$, and a T-independent term that varies between compounds, corresponding to $3k_B[\ln(k_B)+1]-k_B\int_0^\infty \ln(\hbar\omega)\Delta g(\omega)d\omega$. These two terms emerge when simplifying the expression for the vibrational entropy leveraging series expansion at high temperature, as detailed in Sec. II. This analysis highlights two important points regarding solid-state vibrational entropy of vacancy formation in the high-temperature regime: (i) the decrease with temperature follows a logarithmic trend [specifically, the form $-3k_B\ln(T)$], and (ii) the differences in ΔS_{vib} between compounds are constant. The values of the non-temperature-dependent component of ΔS_{vib} accounting for the differences between compounds are reported in Table I.

The compounds' vibrational entropies of vacancy formation can also be further analyzed by artificially eliminating the difference in the number of atoms between pristine and defective cells. An estimate of the vibrational entropy of vacancy formation entirely excluding the contribution from the oxygen atom becoming vacant can be obtained by first computing the atomic projections of the vibrational entropy of the pristine cell, then calculating their sum excluding the contribution from the O becoming vacant, and finally subtracting the result from the vibrational entropy of the vacancy containing cell. Such a computation, resulting in the pristine cell having the same number of atoms as the defective cell, results in the entropy difference plateauing to positive values after the initial growth, leaving the ranking between compounds unchanged (see Fig. S4).

B. Atomic contributions to ΔS_{vib}

After a brief look at the general characteristics of the contribution of different atoms in the structure to the phonon density of states presented in the previous section for an exemplary material ($HoMnO_3$), the present section provides an in-depth look at the atomic contributions to the vibrational entropy of all compounds included in the study. The analysis is carried out by first grouping the atoms based on their distance to the vacancy, and then examining them singularly. A and B cations are differentiated from O anions, and changes in charge localization and bond length are included in the discussion. The results displayed and discussed in this section pertain to the high-temperature range. The presence of a temperature-dependent contribution to the high-temperature form of ΔS_{vib} [see Eq. (6)] discussed in the previous section is connected to the difference in the number of atoms between pristine and defect-containing cells. In this section, the contributions to ΔS_{vib} are computed separately for each individual atom, and therefore they do not contain a significant temperature dependence at high temperature.

Figure 4 displays the per-atom contribution to ΔS_{vib} ($\Delta S_{\text{vib}}^{\text{atom}}$) for the different atoms in each compound, with the atoms being clustered in six different groups (eight groups for double perovskites): (i) the A cations neighboring the O vacancy site, referred to as "A NN," (ii) the B cations neighboring the O vacancy site, referred to as "B NN" [and, for double perovskites, (ii.i) the B′ cations for neighboring the O vacancy site, referred to as "B′ NN", where "B" indicates Mn and "B"' indicates Ti], (iii) the O anions bonded to the A and B cations neighboring the vacancy, referred to as "O 2NN," (iv) all other A cations, referred to as "A other," (v) all other B cations, referred to as "B other" [and, for double perovskites, (v.i) all other B′ cations, referred to as "B′ other"], and (vi) all other O cations, referred to as "O other." The histograms are color-coded to indicate the number of atoms in each group (darker colors indicating more atoms), and, once again, the figure is divided into subfigures grouping the compounds by structure type: (a) "$LuMnO_3$"-type, (b) pyrochlore, and (c) perovskite.

Comparing different compounds, multiple commonalities and differences in the contributions to the vibrational entropy from each group of atoms can be highlighted. First, in all cases, the largest per-atom contribution to ΔS_{vib} is associated with the cations neighboring the vacancy, with a second sizable contribution coming from the O atoms bonded to those cations. Significant variations can, however, be observed in both the magnitude and the sign of the contributions from the cations' nearest neighbors to the O vacancy. Fe-based perovskites, for example, show a larger "B NN" contribution compared to Mn-based perovskites. The larger value of ΔS_{vib} in $LaMnO_3$ and $CaMnO_3$ compared to $YFeO_3$ and $LaFeO_3$ can be attributed to the largest contributions from "O 2NN" atoms and non-nearest-neighbor cations, which, despite their smaller per-atom contribution compared to NN cations, are larger in number (see Fig. S5). Mn-based double perovskites, on the other hand, show a large positive contribution from the Mn nearest neighbor, but, concurrently, a large negative contribution from the Ti nearest neighbor. A consistently larger "A NN" contribution can be identified in Mn-based "$LuMnO_3$"-type compounds compared to perovskites, with the "B NN" contribution being significantly larger in $LuMnO_3$ than in $YMnO_3$ and $HoMnO_3$. Finally, the pyrochlore $Lu_2Mn_2O_7$ displays a large positive "B NN" contribution and an equally large but negative "A NN" contribution.

To gain deeper insight into the origin of the different features highlighted in Fig. 4, we plot in Fig. 5 all the $\Delta S_{\text{vib}}^{\text{atom}}$ contributions from individual atoms separately (i.e., to each atom corresponds a single data point). We correlate $\Delta S_{\text{vib}}^{\text{atom}}$ to the change in average vibrational frequency of each atom upon vacancy formation ($\Delta\langle\omega^{\text{atom}}\rangle$), and we also discuss changes in charge localization and bond lengths. In this instance, the

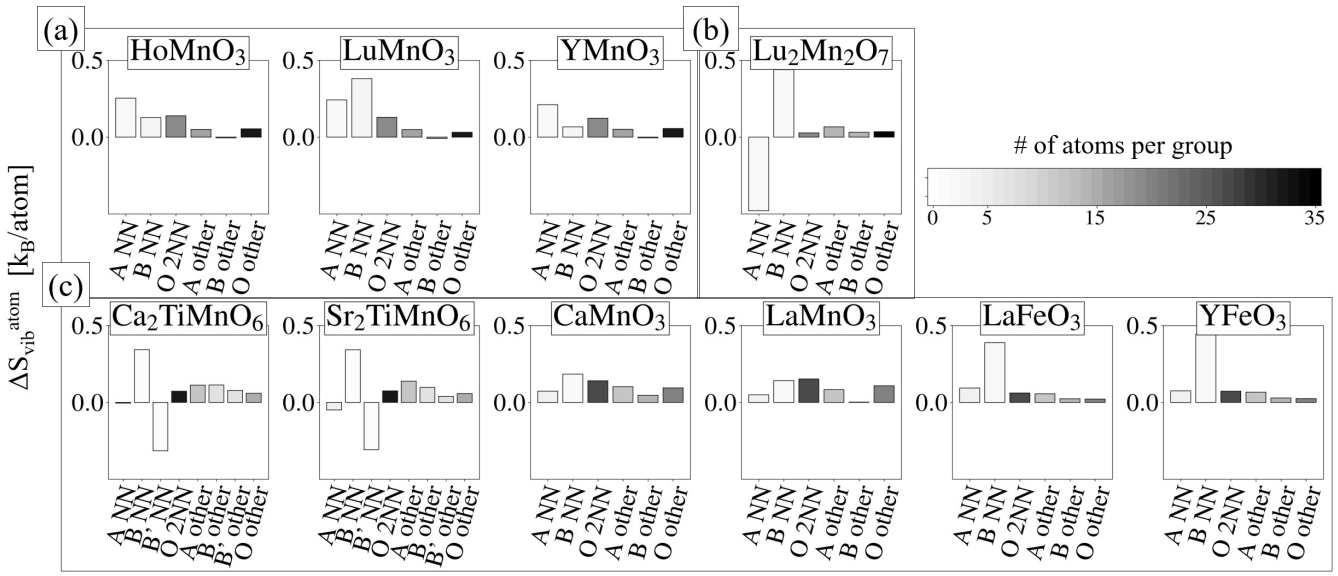

FIG. 4. Per-atom contribution to the solid-state vibrational entropy of O vacancy formation in (a) "$LuMnO_3$"-type, (b) pyrochlore, and (c) perovskite structures. Atoms are divided into six groups (eight groups for double perovskites): (i) the *A* cations neighboring the O vacancy site, referred to as "A NN," (ii) the B cations neighboring the O vacancy site, referred to as "B NN" [and, for double perovskites, (ii.i) the B′ cations for neighboring the O vacancy site, referred to as "B′ NN," where "B" indicates Mn and "B′" indicates Ti), (iii) the O anions bonded to the A and B cations neighboring the vacancy, referred to as "O 2NN," and (iv) all other A cations, referred to as "A other," (v) all other B cations, referred to as "B other" [and, for double perovskites, (v.i) all other B′ cations, referred to as "B′ other"], and (vi) all other O cations, referred to as "O other." Histogram colors indicate the number of atoms in each group (darker colors indicating more atoms).

data points are color-coded based on the average vibrational frequency of the atom of interest in the pristine structure ("$\langle\omega^{\text{atom}}_{\text{BULK}}\rangle$"). The marker shapes are then chosen to distinguish A cations (squares), B cations (diamonds), and O anions (circles), with a superimposed star to mark the A and B cations neighboring the vacancy (those referred to as "A NN," "B NN," and "B′ NN" in Fig. 4), and a superimposed asterisk to mark the O anions bonded to the cations neighboring the vacancy (those referred to as "O 2NN" in Fig. 4). We recognize once again some of the features previously identified in Fig. 4, but we also observe additional details.

In general, a strong correlation between the change in the average vibrational frequency associated with each atom ($\Delta\langle\omega^{\text{atom}}\rangle$) and its contribution to the solid-state vibrational entropy of vacancy formation ($\Delta S^{\text{atom}}_{\text{vib}}$) can be

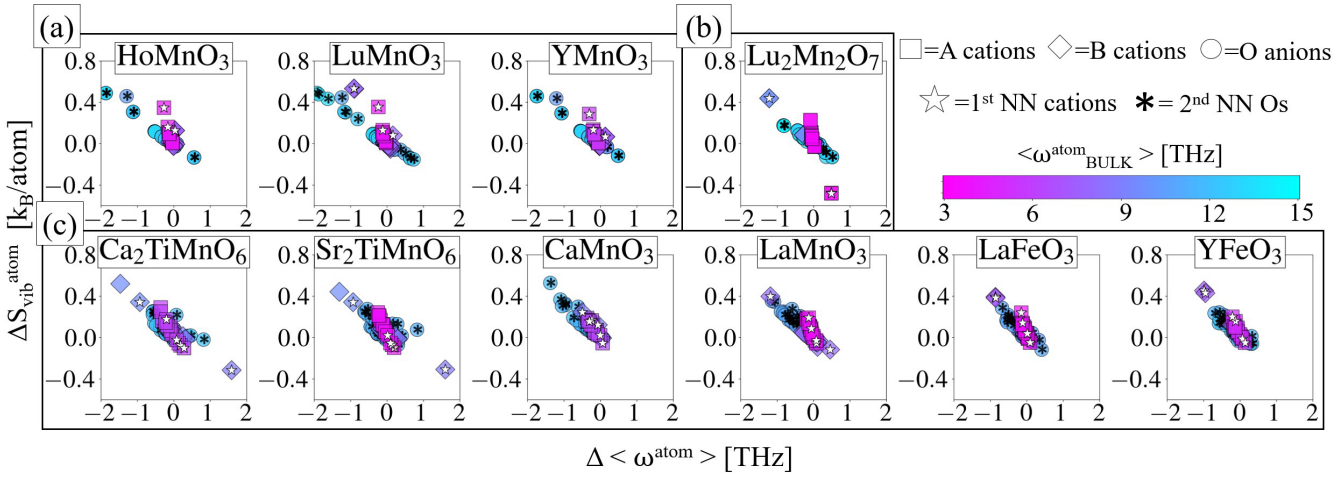

FIG. 5. Per-atom contribution to the solid-state vibrational entropy of O vacancy formation in (a) "$LuMnO_3$"-type, (b) pyrochlore, and (c) perovskite structures, as a function of change in average vibrational frequency of each atom upon vacancy formation. Each data point represents a single atom in the compound, color-coded based on the average vibrational frequency of the atom of interest in the pristine structure ("$\langle\omega^{\text{atom}}_{\text{BULK}}\rangle$"). The marker shapes distinguish A cations (squares), B cations (diamonds), and O anions (circles), with a superimposed star to mark the A and B cations neighboring the vacancy (those referred to as "A NN," "B NN," and "B′ NN" in Fig. 4), and a superimposed asterisk to mark the O anions bonded to the cations neighboring the vacancy (those referred to as "O 2NN" in Fig. 4).

observed: atoms experiencing stronger redshifts in frequency give a stronger positive contribution to ΔS_{vib}, and the opposite for blueshifts. A second correlation between ΔS_{vib} and the average vibrational frequency associated with each atom prior to defect formation ("$\langle\omega^{\text{atom}}_{\text{BULK}}\rangle$") can also be observed. Specifically, for the same change in frequency, atoms with contributions dominating the lower frequency range (A cations) have a larger impact on the vibrational entropy than atoms with contributions dominating the higher-frequency range (O anions). In other words, if a line were to be fitted to the data points belonging to each group of atoms in Fig. 5, the line associated with A atoms would be steeper than that associated with O atoms. The presence of color-coding based on "$\langle\omega^{\text{atom}}_{\text{BULK}}\rangle$" also allows to observe differences in vibrational frequencies among each group (i.e., among A cations, B cations, and O anions). In addition to more evident observations, such as heavier A cations like Lu vibrating at lower frequencies than much lighter cations like Ca, more subtle differences can also be observed. Among the "$LuMnO_3$"-type compounds, for example, Y cations are associated with visibly higher vibrational frequencies compared to Ho and Lu, in accordance with the lower ΔS_{vib} of $YMnO_3$ compared to $LuMnO_3$ and $HoMnO_3$. This feature can also be noticed when comparing the integrated Δ DOS of the three compounds (see Fig. S6) in the very low-frequency range, where $LuMnO_3$ and $HoMnO_3$ have an almost identical trend, with an initial growth starting at lower frequencies than $YMnO_3$.

Having discussed general aspects of the correlation between $\Delta S^{\text{atom}}_{\text{vib}}$ and $\Delta\langle\omega^{\text{atom}}\rangle$), we now concentrate on the individual contributions from different atom types in each structure. On the whole, we again recognize the cations neighboring the vacancy, and the O atoms bonded to them, as the ones associated with the most sizable per-atom contributions to ΔS_{vib}. However, differences between B and A cations within the same compound, and between compounds, are evident.

Focusing first on the B-site cations, we observe a lengthening of the majority of B-O bonds of the B cations neighboring the O vacancy, consistent with the localization of charge on such cations (the ones getting reduced) upon vacancy formation. The significant frequency redshift (and consequent positive contribution to ΔS_{vib}) observed for the B atoms neighboring V_{O} is therefore not only related to the breaking of their bond to the oxygen atom that becomes vacant, but also to the softening of many of their bonds to the other neighboring O atoms. Larger $\Delta S^{\text{atom}}_{\text{vib}}$ and $\Delta\langle\omega^{\text{atom}}\rangle$ are associated with a larger change in the cation's magnetic moment, consistent with a larger change in the charge localized on the atom upon vacancy formation. $LaFeO_3$, $YFeO_3$, Ca_2TiMnO_6, Sr_2TiMnO_6, and $Lu_2Mn_2O_7$, which exhibit the largest contribution from B cations neighboring the vacancy, all display changes in the magnetic moment by $\sim$0.6–0.7μ_B on each "B NN" Fe or Mn cation, while the magnetic moment of two Mn atoms neighboring the vacancy in $LaMnO_3$ and $CaMnO_3$ changes by an average $\sim 0.3\mu_B$. Similarly, while the Mn atoms neighboring the vacancy in $YMnO_3$ and $HoMnO_3$ display a change in magnetic moment of around $\sim 0.1\mu_B$, in $LuMnO_3$, two of the three Mn atomic neighboring the vacancy (the ones with the largest visible frequency redshift) change by about $\sim 0.4\mu_B$. Furthermore, the only large per-atom contribution to ΔS_{vib} associated with a cation not neighboring the O vacancy can be observed in double perovskite oxides, and corresponds to the second Mn cation where the majority of the charge localizes upon vacancy formation (the first Mn cation where charge localizes being the one neighboring the vacancy). The large decrease in the average vibrational frequency of this second Mn cation can once again be traced back to the lengthening of the bonds to its neighboring O anions resulting from the additional negative charge localized on it. On the opposite end to what was just observed, the absence of significant charge localizing on the Ti cation neighboring the vacancy in the two double perovskite oxides can be related to its $\Delta S^{\text{atom}}_{\text{vib}}$ contribution opposing that of the Mn atom neighboring the vacancy. Despite the breaking of the bond between the Ti atom and the oxygen becoming vacant, the shortening of the remaining Ti-O bonds appears to result in a dominant negative contribution ΔS_{vib}, and blueshift of the average vibrational frequency associated with the Ti atom.

Differently from the B cations described above, no sizable change in the charge localized on the A cations neighboring the vacancy is observed upon V_{O} formation. While still experiencing bond breaking, the change in length of the remaining A-O bonds varies in sign, resulting often in smaller "A NN" $\Delta S^{\text{atom}}_{\text{vib}}$ values compared to the ones associated with "B NN." The compounds for which the most sizable "A NN" contributions can be observed are the three "$LuMnO_3$"-type oxides, and the pyrochlore oxide. In the first case, the breaking of the bond between the oxygen becoming vacant and its closest A cation results in a shift of such a cation in the opposite direction to the previously occupied O site. Such a shift is accompanied by a mixed shortening and lengthening of the remaining A-O bonds, with the bonds becoming longer, however, coinciding with the ones associated with longitudinal force constants of greater magnitude, an observation in line with the overall positive contribution to ΔS_{vib}. In pyrochlore $Lu_2Mn_2O_7$, on the other hand, upon the breaking of the Lu-O bond of the two Lu atoms nearest to V_{O}, a shortening of the remaining Lu-O bonds can be observed across the board, resulting in an overall negative contribution to ΔS_{vib}.

C. Influence of Hubbard U on ΔS_{vib}

DFT calculations of metal oxides containing 3D transition metals, like the ones studied in this work, suffer from an over-delocalization of electrons brought about by the residual self-interaction present in exchange-correlation functionals. The addition of a Hubbard-like term to the energy functional [33–38], which carries a very limited additional computational cost, is a widely employed strategy to address this issue, and the one utilized in the present work. The value of the U parameter contained in the Hubbard term can have sizable effects on different properties, and optimal values vary with the transition metal of interest and with the local environment in which it is immersed [44].

We investigate here the influence of different U values on the vibrational entropy of vacancy formation of different compounds. Given the significant computational expense involved in each ΔS_{vib} calculation, we perform this investigation for a subset of the compounds, spanning different structures, and different identities and oxidation states of the

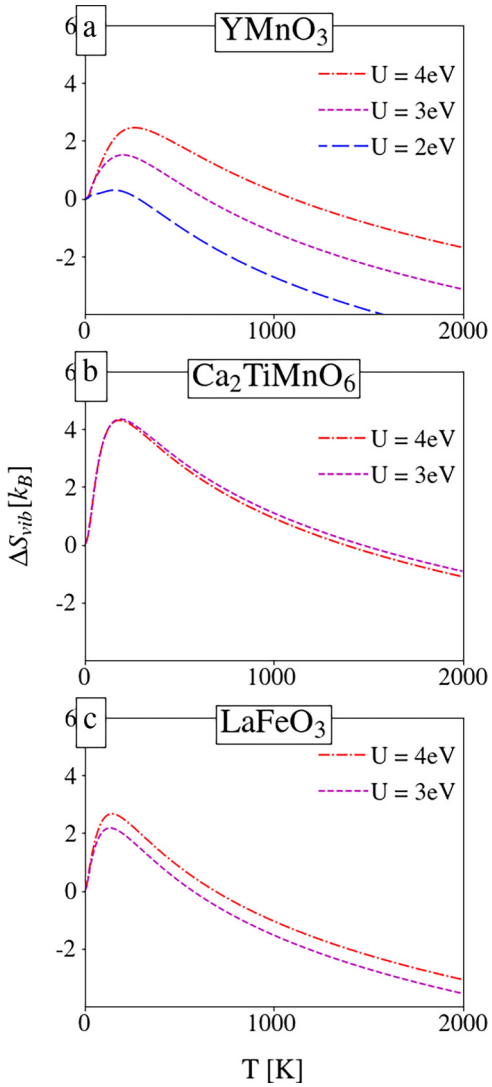

FIG. 6. Change in solid-state vibrational entropy with temperature for different Hubbard U values for (a) $YMnO_3$, (b) Ca_2TiMnO_3, and (c) $LaFeO_3$.

3D transition-metal B cations. As shown in Fig. 6, the largest change in vibrational entropy with U value can be observed for $YMnO_3$, with Ca_2TiMnO_6 and $LaFeO_3$ displaying small to negligible differences between U values. Examining the individual atomic contributions to the vibrational entropy of defect formation (see Fig. S7), it appears that for $YMnO_3$, a decrease in U value leads to lower contributions across the board, while Ca_2TiMnO_6 and $LaFeO_3$ display very little response to changes in U on all atomic contributions.

D. Total entropy of O vacancy formation

Having examined the change in solid-state vibrational entropy upon vacancy formation in the previous sections, we now discuss other sources of entropy playing a significant role in the total entropy of vacancy formation. As mentioned in Sec. II, ΔS_{vib} only includes vibrational contributions from the metal oxide itself, and does not account for the final gaseous state of the oxygen being lost by the metal oxide. Therefore,

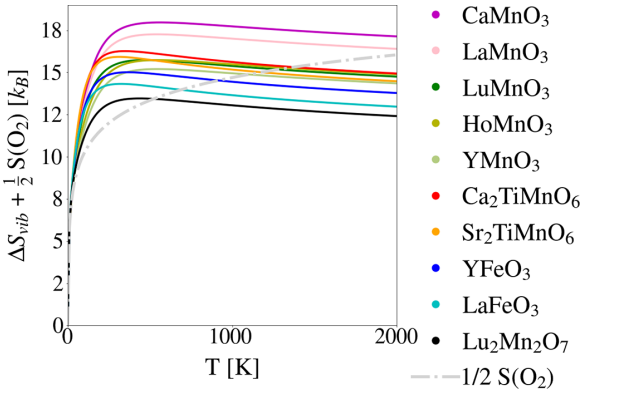

FIG. 7. Sum of the solid-state vibrational entropy of O vacancy formation (ΔS_{vib}), and the gas entropy of oxygen [1/2 $S(O_2)$] as a function of temperature for the compounds investigated in Secs. III A and III B (that have O vacancy concentrations of, respectively, ∼2.1% for perovskites, ∼1.9% for "$LuMnO_3$"-type compounds, and ∼1.8% for pyrochlore).

the oxygen gas entropy is the first contribution we discuss in the present section. Furthermore, the multiplicity of sites upon which defects can be introduced results in an additional, defect concentration-dependent contribution to the total entropy, in the form of configurational entropy.

The oxygen gas entropy can be accounted for as half of the gas entropy of the O_2 molecules, and it can be extracted from tabulated standard values [40]. Figure 7 displays the derived nonconfigurational entropy of O vacancy formation, computed by combining the gas entropy and the solid-state vibrational entropy contributions. In all cases, in addition to the visible dominance of the gas entropy contribution, the temperature dependences of ΔS_{vib} and $\Delta S(O_2)$ can also be observed to counterbalance each other, leading to an almost constant value of the nonconfigurational entropy above room temperature.

The high-temperature behavior of the combination of oxygen gas and solid-state vibrational entropy components can in fact be simply outlined and understood *a priori* considering the high-temperature form of the two terms. As seen in Sec. III A, in the high-temperature range, ΔS_{vib} follows the form $-3k_B \ln(T)$ (visualized in Fig. S8 b). In the same temperature range, the overall temperature dependence of $\frac{1}{2}\Delta S(O_2)$ is captured by the term $\frac{9}{4}k_B \ln(T)$ (visualized in Fig. S8 a). When summed, the two temperature-dependent components of $\frac{1}{2}\Delta S(O_2)$ and ΔS_{vib} largely counterbalance each other, leading the temperature dependence of the nonconfigurational entropy term to follow the form of $-\frac{3}{4}k_B \ln(T)$. Therefore, it is a general result (at the harmonic level) that the influence of temperature becomes much weaker when combining the gas and solid-state vibrational entropy of oxygen vacancy formation compared to any of the two separately, as illustrated in Fig. 8.

The configurational entropy associated with the formation of oxygen vacancies can be computed analytically assuming dilute solution behavior. In this case, the per-vacancy contribution is a function of the nonstoichiometry δ, which varies depending on the available sites, and, if relevant, on the energy difference between them. For the compounds included in this

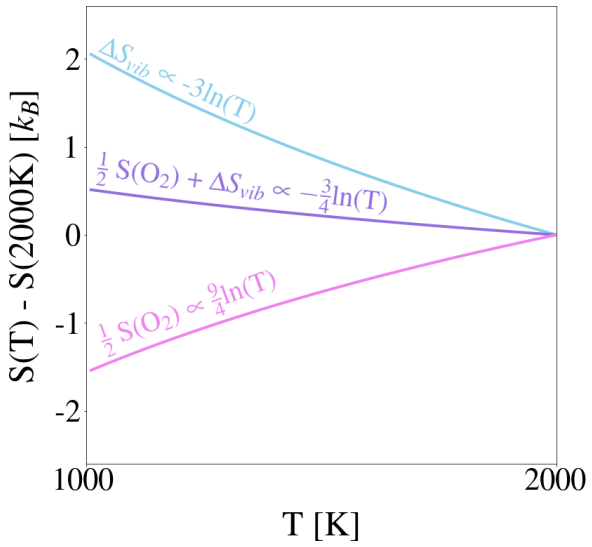

FIG. 8. High-temperature form of the temperature dependence of the solid-state vibrational entropy of O vacancy formation ΔS_{vib} (light blue), the oxygen gas entropy (pink), and their sum (violet), illustrated in the temperature range between 1000 and 2000 K, with respect to the value of each term at 2000 K.

study, and for nonstoichiometry values between $\delta = 0.01$ and 0.1, this results in values ranging between $\sim 6k_B$ and $\sim 3k_B$. In addition to multiplicity of configurations associated with the oxygen vacancy, a similar reasoning can be applied to the cations undergoing reduction, with again configurational entropy values depending on possible sites (e.g., for the compounds in this study, sites on the A sublattice are not included as they do not show evidence of reduction, but reduction on both the A and B sublattices can be observed in other cases [45]). Considering all B sites, aside from the ones occupied by Ti atoms in double perovskites, for nonstoichiometry values between $\delta = 0.01$ and 0.1, this additional entropy contribution varies between $\sim 1k_B$ and $\sim 8k_B$ for the compounds in this study. It should be noted, however, that deviations from ideal values of the configurational entropy can often be observed as a result of phenomena such as interactions between defects [25].

Entropies of reduction for a number of the compounds investigated in this work were reported in recent experimental studies by Qian *et al.* [46–49] and Mastronardo *et al.* [50]. Comparison between computational results and experimental data is, however, complicated by multiple factors. First, the three "$LuMnO_3$"-type compounds displayed evidence of a phase transition to a (dynamically unstable at 0 K) "Be_3N_2"-type structure, with a jump in the extracted thermodynamic quantities of reduction, the origin of which remains unexplained [18,46]. $LaMnO_3$ was synthesized in a rhombohedral perovskite structure (rather than the orthorhombic DFT ground state), dynamically unstable at 0 K (therefore making the computation of the vibrational entropy challenging). Both $CaMnO_3$ and Ca_2TiMnO_6 were also observed to undergo a phase transition, in this case to the cubic perovskite phase (again dynamically unstable at 0 K), leaving only a small range of values for which oxygen loss was measured from the ground-state distorted perovskite structure. Furthermore, cation disorder on the B lattice was experimentally observed in both Ca_2TiMnO_6 and Sr_2TiMnO_6. Finally, $YFeO_3$ displayed very limited oxygen loss, impacting the accuracy of the extracted entropy and enthalpy of reduction. In addition to the just mentioned complications, the experimental uncertainties of $0.5-2.5k_B$ are comparable in magnitude to differences between compounds in our calculated vibrational entropies, and the impact of potential deviations from the ideal configurational entropy represents an additional source of uncertainty in the total entropy calculation.

IV. CONCLUSION

The present work is dedicated to an investigation of the solid-state vibrational entropy of oxygen vacancy formation ΔS_{vib} across a range of 10 metal oxide compounds with different structure types. The computation is carried out by taking the difference between a defect-containing and a pristine cell, and accounting for the final gaseous state of oxygen separately, through a gas term discussed in the last section of the text. We first examine the trend in ΔS_{vib} with temperature, finding common features between all compounds: an initial increase until around room temperature, followed by a steady decrease, due to the presence of an additional oxygen atom (the one becoming vacant) in the pristine structure. Investigating the role of individual atoms, we highlight largely positive contributions to ΔS_{vib} from the cations neighboring the vacancy and the O atoms bonded to them. We also examine changes in bonding and charge localization, and we observe the B cations on which the majority of change localizes upon vacancy formation to experience an average lengthening of their bonds to the neighboring anions. Finally, we consider oxygen gas and configurational contributions to the total entropy of vacancy formation. We show the temperature dependence of the gas entropy to largely counterbalance that of the vibrational entropy, leading to an almost temperature-independent nonconfigurational entropy of vacancy formation at high temperature. We also observe the solid-state vibrational contribution to be significantly smaller than that from oxygen gas and dilute configurational entropy, albeit non-negligible.

ACKNOWLEDGMENTS

This work was funded by the U.S. Department of Energy under Grant No. DE-EE0008089. The calculations were performed relying on the computing power provided by the Quest high-performance computing facility at Northwestern University, and computational resources at the National Energy Research Scientific Computing Center (NERSC), a U.S. Department of Energy Office of Science User Facility, under Contract No. DE-AC02-05CH11231.

[1] H. Tan, Z. Zhao, W.-b. Zhu, E. N. Coker, B. Li, M. Zheng, W. Yu, H. Fan, and Z. Sun, ACS Appl. Mater. Interfaces **6**, 19184 (2014).

[2] M. Ji, J. H. Kim, C.-H. Ryu, and Y.-I. Lee, Nano Energy **95**, 106993 (2022).

[3] T. Nakamura, Sol. Energy **19**, 467 (1977).

[4] Z. Wang, R. Roberts, G. Naterer, and K. Gabriel, Int. J. Hydrogen Energy **37**, 16287 (2012).

[5] A. H. McDaniel, E. C. Miller, D. Arifin, A. Ambrosini, E. N. Coker, R. O'Hayre, W. Chueh, and J. Tong, Energy Environ. Sci. **6**, 2424 (2013).

[6] A. McDaniel, A. Ambrosini, E. Coker, J. Miller, W. Chueh, R. O'Hayre, and J. Tong, Energy Proc. **49**, 2009 (2014).

[7] J. R. Scheffe, D. Weibel, and A. Steinfeld, Energy Fuels **27**, 4250 (2013).

[8] J. Vieten, B. Bulfin, D. E. Starr, A. Hariki, F. M. F. deGroot, A. Azarpira, C. Zachäus, M. Hävecker, K. Skorupska, N. Knoblauch, M. Schmücker, M. Roeb, and C. Sattler, Energy Technol. **7**, 131 (2019).

[9] M. Roeb, M. Neises, N. Monnerie, F. Call, H. Simon, C. Sattler, M. Schmuker, and R. Pitz-Paal, Materials **5**, 2015 (2012).

[10] M. Ezbiri, M. Takacs, B. Stolz, J. Lungthok, A. Steinfeld, and R. Michalsky, J. Mater. Chem. A **5**, 15105 (2017).

[11] B. Meredig and C. Wolverton, Phys. Rev. B **80**, 245119 (2009).

[12] S. B. Adler, Chem. Rev. **104**, 4791 (2004).

[13] J. A. Kilner and M. Burriel, Annu. Rev. Mater. Res. **44**, 365 (2014).

[14] R. B. Wexler, G. S. Gautam, E. B. Stechel, and E. A. Carter, J. Am. Chem. Soc. **143**, 13212 (2021).

[15] A. A. Emery, J. E. Saal, S. Kirklin, V. I. Hegde, and C. Wolverton, Chem. Mater. **28**, 5621 (2016).

[16] A. M. Deml, V. Stevanovic, C. L. Muhich, C. B. Musgrave, and R. O'Hayre, Energy Environ. Sci. **7**, 1996 (2014).

[17] A. M. Deml, A. M. Holder, R. P. O'Hayre, C. B. Musgrave, and V. Stevanovic, J. Phys. Chem. Lett. **6**, 1948 (2015).

[18] B. Baldassarri, J. He, X. Qian, E. Mastronardo, S. S. Griesemer, S. Haile, and C. Wolverton, Phys. Rev. Mater. **7**, 065403 (2023).

[19] M. D. Witman, A. Goyal, T. Ogitsu, A. H. McDaniel, and S. Lany, Nat. Comput. Sci. **3**, 675 (2023).

[20] Z. Wan *et al.*, Phys. Chem. Chem. Phys. **23**, 15675 (2021).

[21] S. Liu *et al.*, ACS Appl. Mater. Interfaces **14**, 11758 (2022).

[22] S. A. Naghavi, A. A. Emery, H. A. Hansen, F. Zhou, V. Ozolins, and C. Wolverton, Nat. Commun. **8**, 285 (2017).

[23] W. C. Chueh, C. Falter, M. Abbott, D. Scipio, P. Furler, S. M. Haile, and A. Steinfeld, Science **330**, 1797 (2010).

[24] Y. Hao, C.-K. Yang, and S. M. Haile, Chem. Mater. **26**, 6073 (2014).

[25] C. B. Gopal and A. van de Walle, Phys. Rev. B **86**, 134117 (2012).

[26] S. Grieshammer, T. Zacherle, and M. Martin, Phys. Chem. Chem. Phys. **15**, 15935 (2013).

[27] P. Agoston and K. Albe, Phys. Chem. Chem. Phys. **11**, 3226 (2009).

[28] T. S. Bjorheim, M. Arrigoni, D. Gryaznov, E. Kotomin, and J. Maier, Phys. Chem. Chem. Phys. **17**, 20765 (2015).

[29] G. Kresse and J. Furthmuller, Comput. Mater. Sci. **6**, 15 (1996).

[30] G. Kresse and J. E. Furthmuller, Phys. Rev. B **54**, 11169 (1996).

[31] G. Kresse and D. Joubert, Phys. Rev. B **59**, 1758 (1999).

[32] J. P. Perdew, M. Burke, and K. Ernzerhof, Phys. Rev. Lett. **77**, 3865 (1996).

[33] B. Himmetoglu, A. Floris, S. de Gironcoli, and M. Cococcioni, Int. J. Quantum Chem. **114**, 14 (2014).

[34] F. Zhou, M. Cococcioni, C. A. Marianetti, D. Morgan, and G. Ceder, Phys. Rev. B **70**, 235121 (2004).

[35] L. Wang, T. Maxisch, and G. Ceder, Phys. Rev. B **73**, 195107 (2006).

[36] S. Lutfalla, V. Shapovalov, and A. T. Bell, J. Chem. Theor. Comput. **7**, 2218 (2011).

[37] V. L. Chevrier, S. P. Ong, R. Armiento, M. K. Y. Chan, and G. Ceder, Phys. Rev. B **82**, 075122 (2010).

[38] S. L. Dudarev, G. A. Botton, S. Y. Savrasov, C. J. Humphreys, and A. P. Sutton, Phys. Rev. B **57**, 1505 (1998).

[39] A. Togo and I. Tanaka, Scr. Mater. **108**, 1 (2015).

[40] T. C. Allison, Nist-janaf thermochemical tables-srd 13 (2013).

[41] B. Fultz, Prog. Mater. Sci. **55**, 247 (2010).

[42] S. J. Blundell and K. M. Blundell, *Concepts in Thermal Physics* (Oxford University Press, Oxford, 2010).

[43] See Supplemental Material at http://link.aps.org/supplemental/10.1103/PhysRevMaterials.8.055407 for additional figures.

[44] M. Aykol and C. Wolverton, Phys. Rev. B **90**, 115105 (2014).

[45] G. Sai Gautam, E. B. Stechel, and E. A. Carter, Chem. Mater. **32**, 9964 (2020).

[46] X. Qian, Nonstoichiometric Perovskite Oxides for Solar-Driven Thermochemical Water Splitting, Ph.D. thesis, Northwestern University, 2021.

[47] X. Qian, J. He, E. Mastronardo, B. Baldassarri, C. Wolverton, and S. M. Haile, Chem. Mater. **32**, 9335 (2020).

[48] X. Qian, J. He, E. Mastronardo, B. Baldassarri, W. Yuan, C. Wolverton, and S. M. Haile, Matter **4**, 688 (2021).

[49] X. Qian, S. M. Haile, T. C. Davenport, and E. Mastronardo, J. Am. Ceram. Soc. **105**, 4375 (2022).

[50] E. Mastronardo, X. Qian, J. M. Coronado, and S. M. Haile, J. Mater. Chem. A **8**, 8503 (2020).